FIG. 12. Box-and-whisker plots of (a) maturation area (10^3 km^2), (b) maximum areal growth rate, (c) average maximum TBB gradient (K km^{-1}), and (d) average TBB$_{min}$ (K). The boxes cover the 25th–75th percentiles, the horizontal lines in the boxes mark the median values, the pentagrams denote the mean values, and the lower and upper whiskers cover the 5th–95th percentiles.

represented by 200, 300, 400, and 500 hPa for C1 and C2 MCSs and by 200, 500, 700, and 850 hPa for C3 and C4 MCSs, respectively. In addition, we eliminated MCSs that were initiated at the same time, and in this study 1026, 834, 360, and 444 MCSs were composited for C1, C2, C3, and C4, respectively.

In the upper troposphere (200 hPa), common features of the four categories of MCSs include an upper-level jet (ULJ, wind speed $\geq$ 30 m s^{-1}) around 40°N and the South Asian High (SAH) controlling those south of 30°N. However, C1 and C3 MCSs are initiated in the south of the ULJ, while C2 and C4 MCSs are more than 1000 km away from the ULJ. The ULJ therefore has little influence on the formation of C2 and C4 MCSs. The main difference is that C1 MCSs are controlled by a straight westerly flow in the north of the SAH, and the C2, C3, and C4 MCSs are controlled by anticyclone circulation in the east of the high pressure. In addition, the SAH related to C2 MCSs is stronger than that for the others, the position of the SAH for C3 MCSs extends further northward than for the other three categories, and the range of the SAH for C4 MCSs is the smallest (Fig. 17).

The composite circulation at the middle level (300 hPa) for C1 and C2 MCSs is similar to that at the upper level (Figs. 18a,b). At 400 hPa, a cyclone appears in the Bay of Bengal and high pressure dominates the south of the Tibetan Plateau, the west of the Indochina Peninsula, and Bangladesh (Figs. 18c,d). The active area of C1 MCSs is still controlled by straight westerly flow in the north of the high-pressure region (Fig. 18c). At 500 hPa, westerly wind still controls the region of the C1 MCSs. The control of the westerly wind in the middle and lower levels is conducive to the eastward propagation of MCSs. In addition, high specific humidity and cyclonic circulation appear in the east of the Sichuan Basin, which is favorable for eastward propagation and long tracking of C1 MCSs (Figs. 18e and 8a). The active area of C2 MCSs is in the east of the high pressure at 400 hPa, which is similar to that at 300 hPa (Fig. 18d). The region of C2 MCSs is in the control of the high pressure at 500 hPa. The wind speed, specific humidity, and moisture content in the active region of C2 MCSs are smaller than those of C1 MCSs (Fig. 18f). Previous studies have revealed that cyclones in the Bay of Bengal can transport more
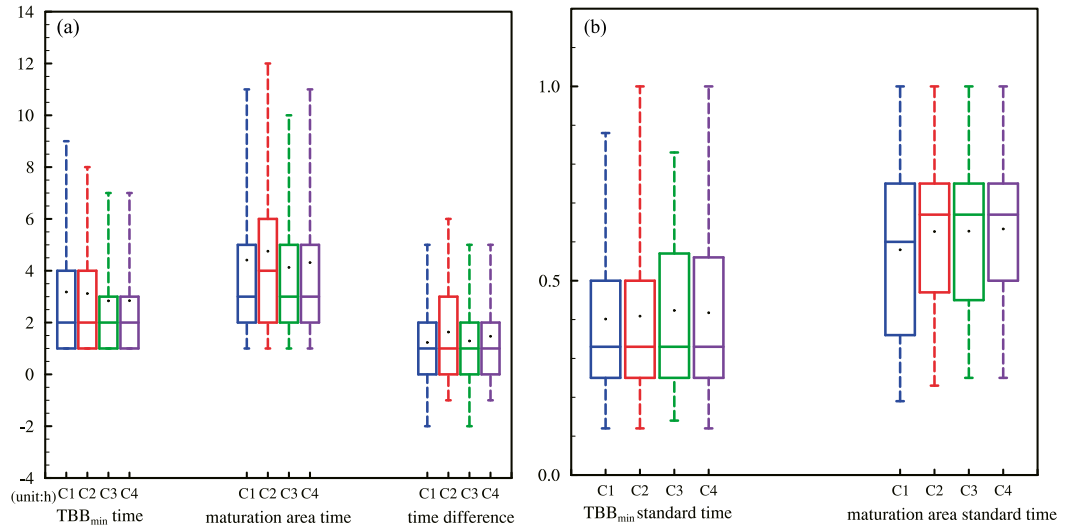
FIG. 13. Box-and-whisker plots of (a) TBB$_{min}$ time, maturation area time, and their time difference, and (b) TBB$_{min}$ standard time and maturation area standard time. The boxes cover the 25th–75th percentiles, the horizontal lines in the boxes mark the median values, the dots denote the mean values, and the lower and upper whiskers cover the 5th–95th percentiles.

water vapor to the plateau area under southwesterly and southerly wind (Xu et al. 2002; Chen et al. 2006). The combination of a cyclone in the Bay of Bengal and high pressure in the west of the Indochina Peninsula and Bangladesh can transport water vapor to the active areas of C1 and C2 MCSs.

At 500 hPa, the cyclones are also active in the Bay of Bengal for C3 and C4 MCSs, which is similar to the C1 and C2 MCSs

(Figs. 19a,b). At the same time, there are relatively small high-pressure activities in the Indochina Peninsula that are much weaker than those of C1 and C2 MCSs. The matching of cyclones in the Bay of Bengal and high pressure in the Indochina Peninsula is more conducive to transporting water vapor from the Bay of Bengal to the active regions of C3 and C4 MCSs. Moreover, cyclonic circulation is stronger for C3 MCSs than
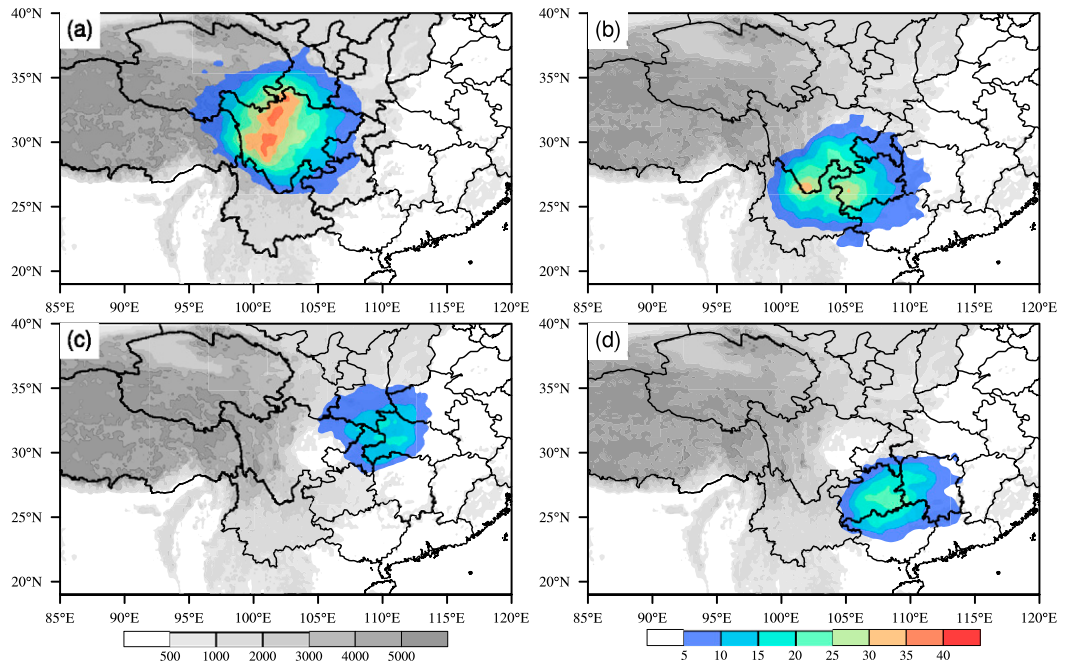
FIG. 14. Contribution rates of MCS-related precipitation to the local total accumulated precipitation of the four categories of MCS during May–September (colored shading; %), showing (a) C1, (b) C2, (c) C3, and (d) C4. Gray shading denotes elevations higher than 500 m.
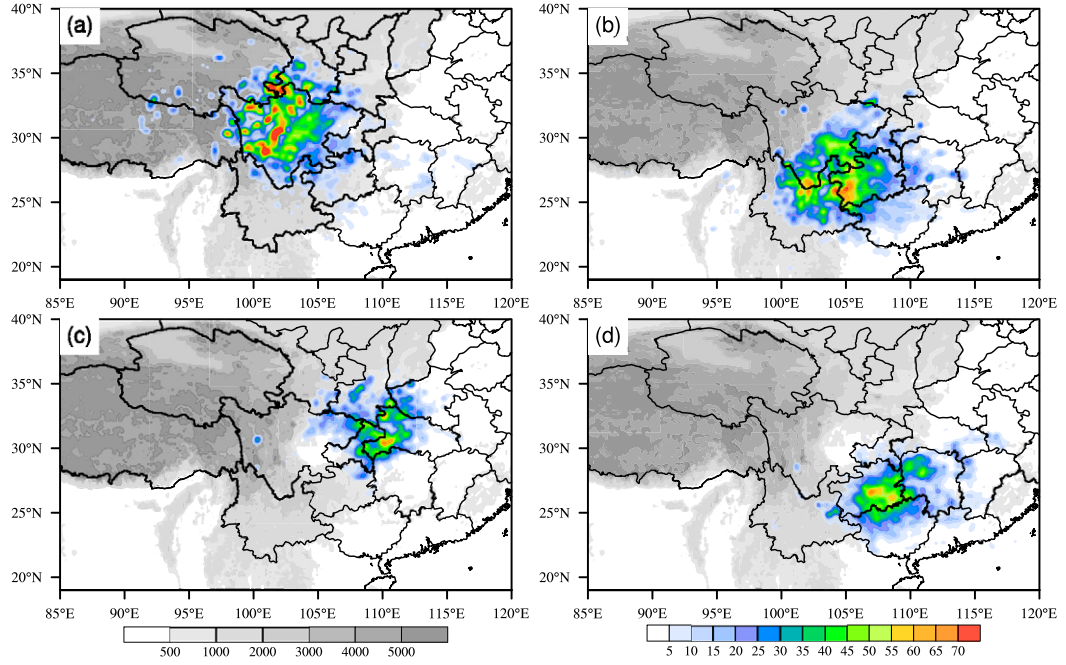
FIG. 15. As in Fig. 14, but for the contribution rate of accumulated precipitation of the four categories of MCS-related SDHR to the local total accumulated precipitation of SDHR.

for C4 MCSs, which could induce water vapor to be transported to the north area (C3 MCSs' active area). The locations of C3 MCSs are controlled by southwesterly airflow ahead of the trough at 500 hPa (Fig. 19a), accompanied with the activity of a vortex at 850 hPa in the western Sichuan Basin (Fig. 19e).

At 850 hPa, the region of C3 MCSs is controlled by a southwesterly wind with a speed of 6 m s^{-1}, and there is a high value of water vapor flux to the south of the active region. The transportation of abundant warmth and moisture flow is beneficial to moisture convergence and results in the formation of
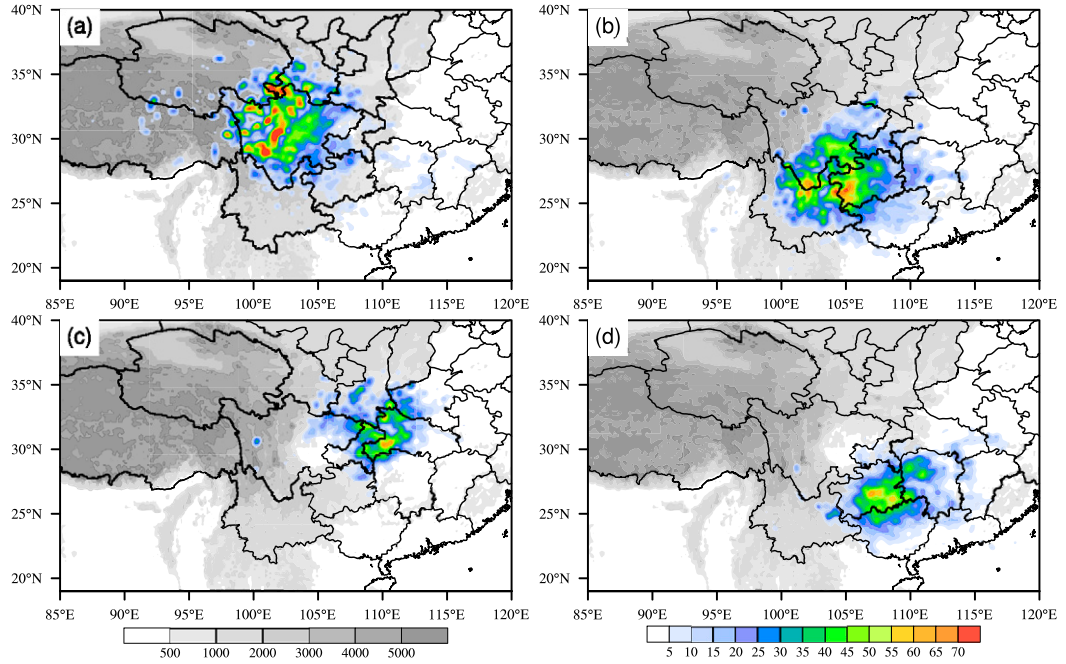
FIG. 16. As in Fig. 15, but for the contribution rate of the frequency of the four categories of MCS-related SDHR to that of the local total frequency of SDHR.
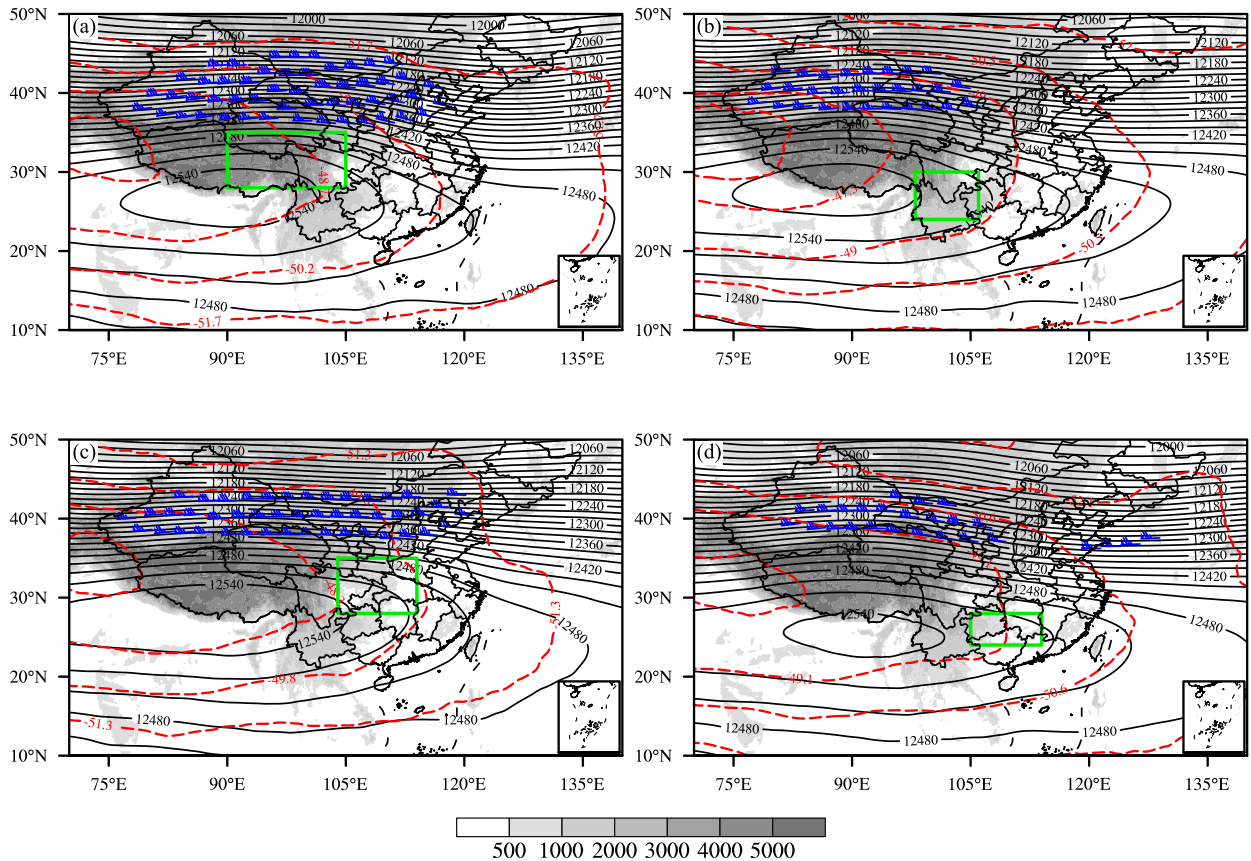
FIG. 17. Composite background circulations for (a) C1, (b) C2, (c) C3, and (d) C4 MCSs at the formation stage at 200 hPa, showing geopotential height (black lines; gpm), temperature (red dotted lines; °C), and wind speeds larger than 30 m s^{-1} (blue wind barbs). The green box denotes the study region, and gray shading denotes elevations higher than 500 m.

convection in the region of the C3 MCSs (Fig. 19e). Compared with the circulations of C3 MCSs, C4 MCSs has weaker cyclonic circulation in the Bay of Bengal and no high pressure in the Indochina Peninsula at 500 hPa (Fig. 19b). The 700 hPa vortex located to the northwest side of the region of the C4 MCSs is not conducive to the northward transportation of moisture, which may be the reason that the active area of C4 MCSs is south of the C3 MCSs (Fig. 19d). The southwest vortex at 850 hPa is active in the northwest of the region of the C4 MCSs, where the high value of water vapor flux in the southeast of the vortex and convergence are favorable for the formation of C4 MCSs (Fig. 19f).

In summary, in the upper troposphere (200 hPa), the four categories of MCSs are controlled by the SAH, while the ULJ (wind speed ≥ 30 m s^{-1}) around 40°N affects only the C1 and C3 MCSs. The cyclone activities in the Bay of Bengal and the high pressure in the Indochina Peninsula in the middle troposphere are the most important systems for the formation of the four types of MCSs, because the matching of these two systems is favorable for the transportation of water vapor to the active area of the MCSs. The locations and intensities of these two systems, either accompanied by a vortex or a southwesterly wind in the low-level troposphere, determine the location and intensity of the convergence

of water vapor flux, which induces the initiation locations of the four types of MCSs.

4. Conclusions and discussions

Based on hourly geostationary satellite data, the MCSs generated in the southwest mountain area (with an elevation ≥ 500 m) during May–September of 2009–18 were identified and tracked. They were then grouped into four categories using K-means clustering based on their location. The main characteristics of the four types of MCSs and their environmental conditions were investigated. The following new findings were obtained.

1) A total of 3059 MCSs of the 2009–18 warm seasons (May–September) initiated over the southwest mountain area with an elevation no less than 500 m were identified and tracked, and these were classified into four categories depending on their initial positions. These MCSs were active and were generated at places across the southwest mountain area. The C1 MCSs were generated in the northeast of the Tibetan Plateau (90°–105°E, 28°–35°N), and then moved eastward, northeastward, or southeastward and matured or terminated in the process of moving to the downstream area. The other three types of MCSs moved mainly
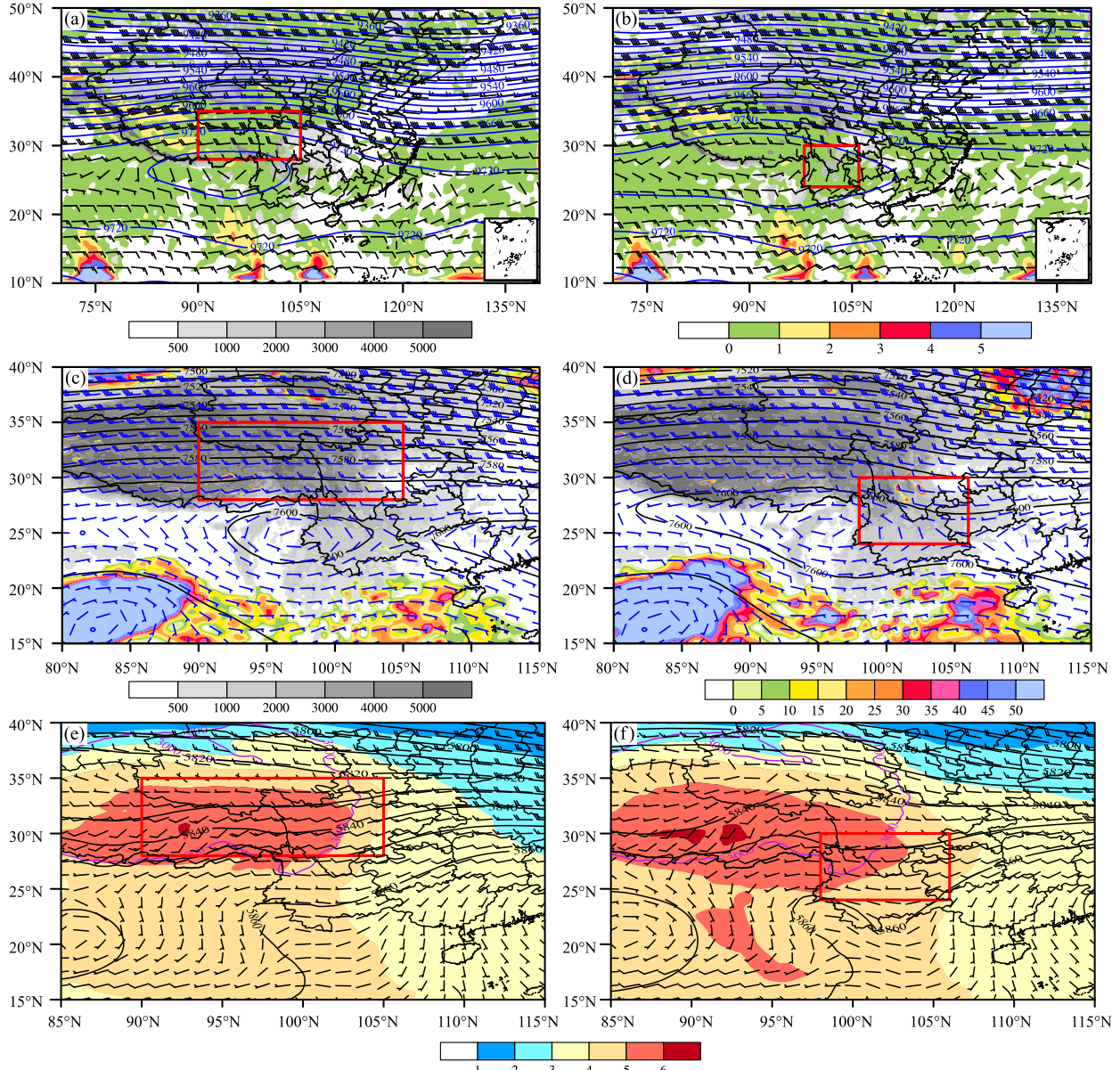
FIG. 18. Composite background circulations for (left) C1 and (right) C2 MCSs at the formation stage at (a),(b) 300; (c),(d) 400; and (e),(f) 500 hPa, showing geopotential height (black lines; gpm) and wind field (wind barbs; 4 m s^{-1}). The red box denotes the study region, gray shading denotes elevations higher than 500 m in (a)–(d), and purple lines are 3000-m elevations in (e) and (f). The color shading in (a) and (b) indicates divergence (10^{-6} s^{-1}), in (c) and (d) this stands for relative vorticity (10^{-6} s^{-1}), and it represents specific humidity (g kg^{-1}) in (e) and (f).

eastward, and a few MCSs moved southwestward. The C2 MCSs were mainly active in the southeast of the Tibetan Plateau and the west of the Yungui Plateau (98°–106°E, 24°–30°N). The C3 and C4 MCSs were active in the Wushan, Qinling, and Ta-pa Mountains (104°–114°E, 28°–35°N) and the Wuling and Xuefeng Mountains (105°–114°E, 24°–28°N), respectively, and they matured or died out in the east, near their site of formation.

2) The four types of MCSs had similar monthly variation and temporal characteristics, which demonstrated a peak in July

and a minimum in May. However, they had different spatial and temporal variations. The majority of the MCSs had a lifespan between 3 and 21 h, but MCSs initiated in the east of the Tibetan Plateau were longer lived than the others. Examination of the diurnal variations of the formation, maturity, and dissipation times showed that the peak of the formation time was 1400–1800 LST, and the maturity–dissipation time was 1600–2300 LST. In addition, C1 and C2 MCSs had a subpeak in their maturity time at 0000–0300 LST and in their dissipation time at 0000–0900 LST.
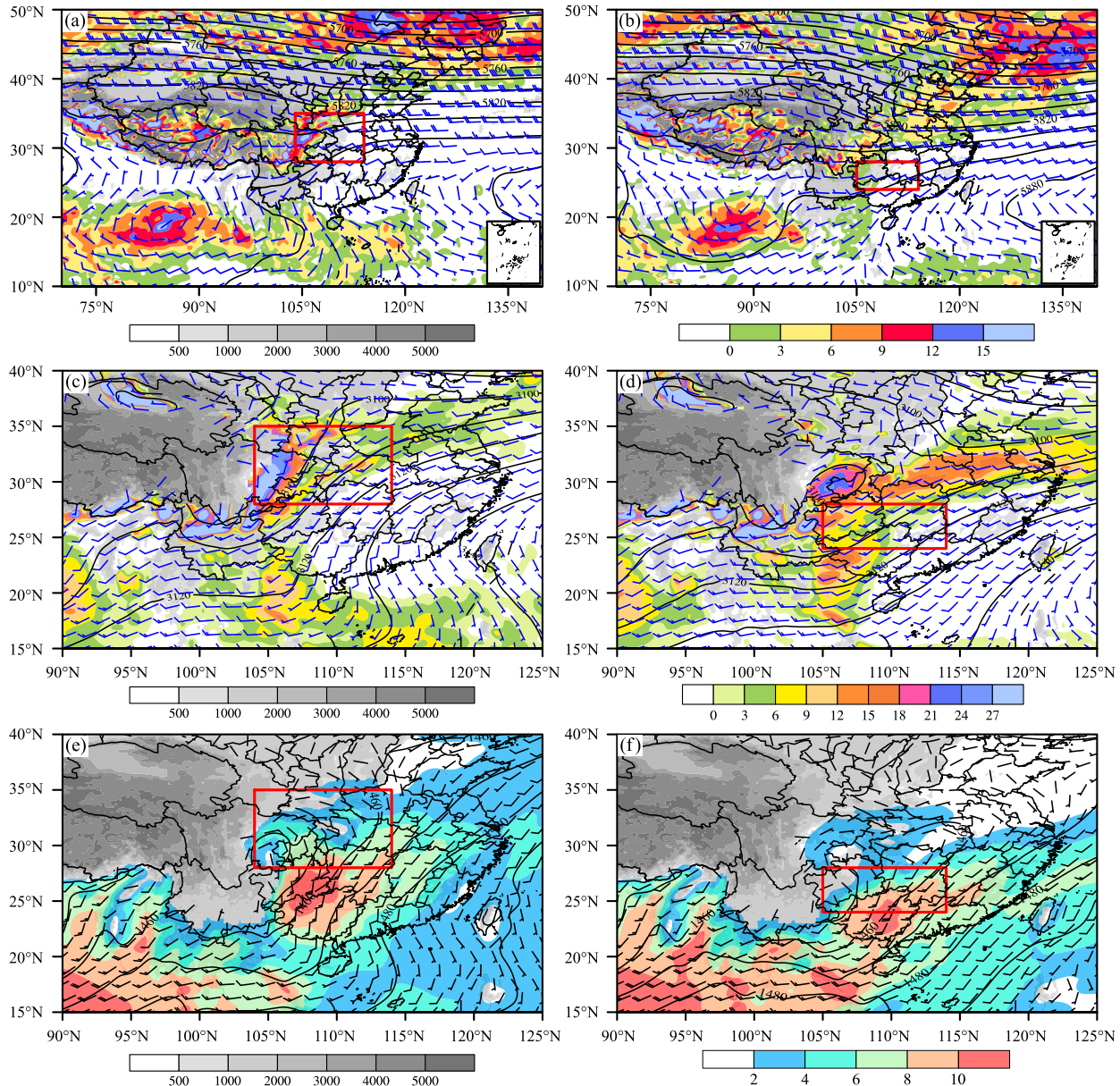
FIG. 19. Composite background circulations for (left) C3 and (right) C4 MCSs at the formation stage at (a),(b) 500; (c),(d) 700; and (e),(f) 850 hPa, showing geopotential height (black lines; gpm) and wind field (wind barbs; 4 m s^{-1}). The red box denotes the study area and gray shading denotes elevations higher than 500 m. The colored shading in (a)–(d) stands for relative vorticity (10^{-6} s^{-1}) and for water vapor flux (g s kg^{-1}) in (e) and (f).

3) On the basis of the analysis of several cloud parameters, the different characteristics during the development of four types MCSs were revealed. The sizes of the MCSs over higher elevations (C1 and C2 types) were larger than those over lower elevations, while the C1 MCSs were the largest and developed more rapidly than the others. However, C2 and C4 MCSs had a larger average maximum TBB gradient and a smaller average TBB$_{min}$, meaning they were stronger than the other two types. Most MCSs attained their TBB$_{min}$ in the first half of their life and reached maturation later. The contribution rates of C1 and C2 MCSs to the total precipitation were

greater than 30%, while those of C3 and C4 MCSs were less than 25%. The contribution rate of MCSs to SDHR was over 60%, and this was mainly influenced by local convection.

4) The ERA5 hourly reanalysis data were employed to reveal major synoptic circulation at the formation time of the four categories of MCSs and distinguish their differences. The formation regions of the four types of MCSs were controlled by the SAH in the upper troposphere, while a ULJ around 40°N affected only the C1 and C3 MCSs. The matching of a cyclone in the Bay of Bengal and high pressure in the Indochina Peninsula in the low-to-middle

troposphere was favorable for the transportation of water vapor to the active areas of the MCSs. The following factors determined the initiation locations of the four types of MCSs: the locations and intensities of cyclones in the Bay of Bengal and high pressure in Indochina Peninsula in the low-to-middle troposphere, and vortexes or south-westerly winds in the low-level troposphere. These factors affect the location and intensity of the convergence of water vapor flux, which regulates the location and intensity of convection.

This statistical study established that the four types of MCSs had different characteristics and each made a large contribution to the SDHR. This indicates that the prediction of local MCSs is critical to the accuracy of forecasts of SDHR. In addition, through compositing, favorable synoptic circulations for the formation of MCSs were compared, but the triggering conditions were not revealed. Therefore, future work should choose a number of cases to study the triggering conditions and their initiation and development mechanisms.

Data availability statement. The data used in this manuscript were obtained from publicly available data repositories: black-body temperature IR1 data were obtained from the Kochi University website at http://weather.is.kochi-u.ac.jp/archive-e.html. GTOPO30 data were available electronically at https://www.usgs.gov/centers/eros/science/usgs-eros-archive-digital-elevation-global-30-arc-second-elevation-gtopo30?qt-science_center_objects=4#qt-science_center_objects. ERA5 data were obtained from the Climate Data Store (https://cds.climate.copernicus.eu/cdsapp#!/search?type=dataset&text=ERA5). COMB data were obtained from the National Meteorological Information Center, China Meteorological Administration (https://data.cma.cn/data/cdcdetail/dataCode/SEVP_CLI_CHN_MERGE_CMP_PRE_HOUR_GRID_0.10.html).

REFERENCES

Ai, Y. F., W. B. Li, Z. Y. Meng, and J. Li, 2016: Life cycle characteristics of MCSs in middle east China tracked by geostationary satellite and precipitation estimates. *Mon. Wea. Rev.*, **144**, 2517–2530, https://doi.org/10.1175/MWR-D-15-0197.1.

Anderson, C. J., and R. W. Arritt, 1998: Mesoscale convective complexes and persistent elongated convective systems over the United States during 1992 and 1993. *Mon. Wea. Rev.*, **126**, 578–599, https://doi.org/10.1175/1520-0493(1998)126<0578:MCCAPE>2.0.CO;2.

Augustine, J. A., and K. W. Howard, 1988: Mesoscale convective complexes over the United States during 1985. *Mon. Wea. Rev.*, **116**, 685–701, https://doi.org/10.1175/1520-0493(1988)116<0685:MCCOTU>2.0.CO;2.

——, and ——, 1991: Mesoscale convective complexes over the United States during 1986 and 1987. *Mon. Wea. Rev.*, **119**, 1575–1589, https://doi.org/10.1175/1520-0493(1991)119<1575:MCCOTU>2.0.CO;2.

Banta, R. M., and C. B. Schaaf, 1987: Thunderstorm genesis zones in the Colorado Rocky Mountains as determined by traceback of geosynchronous satellite images. *Mon. Wea. Rev.*, **115**, 463–476, https://doi.org/10.1175/1520-0493(1987)115<0463:TGZITC>2.0.CO;2.

Bao, X. H., and F. Q. Zhang, 2013: Impacts of the mountain-plains solenoid and cold pool dynamics on the diurnal variation of precipitation over Northern China. *Atmos. Chem. Phys.*, **13**, 6965–6982, https://doi.org/10.5194/acp-13-6965-2013.

Blamey, R. C., and C. J. Reason, 2013: The role of mesoscale convective complexes in southern Africa summer rainfall. *J. Climate*, **26**, 1654–1668, https://doi.org/10.1175/JCLI-D-12-00239.1.

Chen, Y., Y. H. Ding, Z. N. Xiao, and H. M. Yan, 2006: The impact of water vapor transport on the summer monsoon onset and abnormal rainfall over Yunnan province in May (in Chinese). *Chin. J. Atmos. Sci.*, **30**, 25–37.

Coniglio, M. C., J. Y. Hwang, and D. J. Stensrud, 2010: Environmental factors in the upscale growth and longevity of MCSs derived from rapid update cycle analyses. *Mon. Wea. Rev.*, **138**, 3514–3539, https://doi.org/10.1175/2010 MWR3233.1.

Cotton, W. R., M. S. Lin, R. L. McAnelly, and C. J. Tremback, 1989: A composite model of mesoscale convective complexes. *Mon. Wea. Rev.*, **117**, 765–783, https://doi.org/10.1175/1520-0493(1989)117<0765:ACMOMC>2.0.CO;2.

Durkee, J. D., and T. L. Mote, 2010: A climatology of warm-season mesoscale convective complexes in subtropical South America. *Int. J. Climatol.*, **30**, 418–431, https://doi.org/10.1002/JOC.1893.

Feng, Z., X. Q. Dong, B. K. Xi, S. A. McFarlane, A. Kennedy, B. Lin, and P. Minnis, 2012: Life cycle of midlatitude deep convective systems in a Lagrangian framework. *J. Geophys. Res.*, **117**, D23201, https://doi.org/10.1029/2012JD018362.

——, R. A. Houze, L. R. Leung, F. F. Song, J. Hardin, J. Y. Wang, W. I. Gustafson, and C. R. Homeyer, 2019: Spatiotemporal characteristics and large-scale environments of mesoscale convective systems east of the Rocky Mountains. *J. Climate*, **32**, 7303–7328, https://doi.org/10.1175/JCLI-D-19-0137.1.

Goyens, C., D. Lauwaet, M. Schröder, M. Demuzere, and N. P. M. Van Lipzig, 2012: Tracking mesoscale convective systems in the Sahel: Relation between cloud parameters and precipitation. *Int. J. Climatol.*, **32**, 1921–1934, https://doi.org/10.1002/joc.2407.

Hane, C. E., C. L. Ziegler, and H. B. Bluestein, 1993: Investigation of the dryline and convective storms initiated along the dry-line: Field experiments during COPS-91. *Bull. Amer. Meteor. Soc.*, **74**, 2133–2145, https://doi.org/10.1175/1520-0477(1993)074<2133:IOTDAC>2.0.CO;2.

He, Z. W., Q. H. Zhang, L. Q. Bai, and Z. Y. Meng, 2016: Characteristics of mesoscale convective systems in central East China and their reliance on atmospheric circulation patterns. *Int. J. Climatol.*, **37**, 3276–3290, https://doi.org/10.1002/joc.4917.

Hersbach, H., and Coauthors, 2019: Global reanalysis: Goodbye ERA-Interim, hello ERA5. *ECMWF Newsletter*, No. 159, ECMWF, Reading, United Kingdom, 17–24, https://www.ecmwf.int/en/elibrary/19027-global-reanalysis-goodbye-era-interim-hello-era5.

Houze, R. A., 2012: Orographic effects on precipitating clouds. *Rev. Geophys.*, **50**, RG1001, https://doi.org/10.1029/2011RG000365.

Hu, L., D. F. Deng, S. T. Gao, and X. D. Xu, 2016: The seasonal variation of Tibetan convective systems: Satellite observation. *J. Geophys. Res. Atmos.*, **121**, 5512–5525, https://doi.org/10.1002/2015JD024390.

——, ——, X. D. Xu, and P. Zhao, 2017: The regional differences of Tibetan convective systems in boreal summer. *J. Geophys. Res. Atmos.*, **122**, 7289–7299, https://doi.org/10.1002/2017JD026681.

Jiang, Z. H., R. Lu, and Y. G. Ding, 2013: Analysis of the high-resolution merged precipitation products over China based on the temporal and spatial structure score indices (in Chinese). *Acta Meteor. Sin.*, **71**, 891–900.

Jin, X., and J. W. Han, 2010: K-means clustering. *Encyclopedia of Machine Learning*. C. Sammut and G. I. Webb, Eds., Springer, 563–564, https://doi.org/10.1007/978-0-387-30164-8_425.

Jirak, I. L., W. R. Cotton, and R. L. McAnelly, 2003: Satellite and radar survey of mesoscale convective system development. *Mon. Wea. Rev.*, **131**, 2428–2449, https://doi.org/10.1175/1520-0493(2003)131<2428:SARSOM>2.0.CO;2.

Kondo, Y., A. Higuchi, and K. Nakamura, 2006: Small-scale cloud activity over the maritime continent and the western Pacific as revealed by satellite data. *Mon. Wea. Rev.*, **134**, 1581–1599, https://doi.org/10.1175/MWR3132.1.

Kuo, J. T., and H. D. Orville, 1973: A radar climatology of summertime convective clouds in the Black Hills. *J. Appl. Meteor.*, **12**, 359–368, https://doi.org/10.1175/1520-0450(1973)012<0359:ARCOSC>2.0.CO;2.

Laing, A. G., and J. M. Fritsch, 1997: The global population of mesoscale convective complexes. *Quart. J. Roy. Meteor. Soc.*, **123**, 389–405, https://doi.org/10.1002/qj.49712353807.

Lane, T. P., and M. W. Moncrieff, 2015: Long-lived mesoscale systems in a low–convective inhibition environment. Part I: Upshear propagation. *J. Atmos. Sci.*, **72**, 4297–4318, https://doi.org/10.1175/JAS-D-15-0073.1.

Laurent, H., L. A. T. Machado, C. A. Morales, and L. Durieux, 2002: Characteristics of the Amazonian mesoscale convective systems observed from satellite and radar during the WETAMC/LBA experiment. *J. Geophys. Res.*, **107**, 8054, https://doi.org/10.1029/2001JD000337.

Li, J., D. H. Wang, and B. Wang, 2012a: Structure characteristics of moist neutral stratification in a mesoscale convective system (in Chinese). *Climatic Environ. Res.*, **17**, 617–627.

——, B. Wang, and D. H. Wang, 2012b: The characteristics of mesoscale convective systems (MCSs) over East Asia in warm seasons. *Atmos. Ocean. Sci. Lett.*, **5**, 102–107, https://doi.org/10.1080/16742834.2012.11446973.

Li, J. Y., X. Y. Shen, D. H. Wang, and J. Li, 2015: Distribution and characteristic of the MCS over South China during the spring and summer of 2008 (in Chinese). *J. Trop. Meteor.*, **31**, 475–485.

Liao, J., B. Xu, and H. Z. Zhang, 2013: Assessment of experiment of merging gauge observations with CMORPH (in Chinese). *J. Trop. Meteor.*, **29**, 163–171.

Lloyd, S. P., 1982: Least squares quantization in PCM. *IEEE Trans. Inf. Theory*, **28**, 129–137, https://doi.org/10.1109/TIT.1982.1056489.

MacQueen, J. B., 1967: Some methods for classification and analysis of multivariate observations. *Proceedings of the Fifth Berkeley Symposium on Mathematical Statistics and Probability*, Vol. 1, L. M. Le Cam and J. Neyman, Eds., University of California Press, 281–297, https://projecteuclid.org/euclid.bsmsp/1200512992.

Maddox, R. A., 1980: Mesoscale convective complexes. *Bull. Amer. Meteor. Soc.*, **61**, 1374–1387, https://doi.org/10.1175/1520-0477(1980)061<1374:MCC>2.0.CO;2.

——, 1983: Large-scale meteorological conditions associated with midlatitude, mesoscale convective complexes. *Mon. Wea. Rev.*, **111**, 1475–1493, https://doi.org/10.1175/1520-0493(1983)111<1475:LSMCAW>2.0.CO;2.

Mai, Z., S. M. Fu, and J. H. Sun, 2019: Statistical features of two types of mesoscale convective systems (MCSs) generated over the eastern Tibetan Plateau during 16 warm seasons (in Chinese). *Climatic Environ. Res.*, **25** (4), 385–398.

——, ——, ——, and L. Hu, 2020: Key statistical characteristics of the mesoscale convective systems generated over the Tibetan Plateau and their relationship to precipitation and southwest vortices. *Int. J. Climatol.*, https://doi.org/10.1002/joc.6735, in press.

Mathon, V., and H. Laurent, 2001: Life cycle of Sahelian mesoscale convective cloud systems. *Quart. J. Roy. Meteor. Soc.*, **127**, 377–406, https://doi.org/10.1002/qj.49712757208.

——, ——, and T. Lebel, 2002: Mesoscale convective system rainfall in the Sahel. *J. Appl. Meteor.*, **41**, 1081–1092, https://doi.org/10.1175/1520-0450(2002)041<1081:MCSRIT>2.0.CO;2.

McAnelly, R. L., and W. R. Cotton, 1992: Early growth of mesoscale convective complexes: A meso-β-scale cycle of convective precipitation? *Mon. Wea. Rev.*, **120**, 1851–1877, https://doi.org/10.1175/1520-0493(1992)120<1851:EGOMCC>2.0.CO;2.

Meisner, B. N., and P. A. Arkin, 1987: Spatial and annual variations in the diurnal cycle of large-scale tropical convective cloudiness and precipitation. *Mon. Wea. Rev.*, **115**, 2009–2032, https://doi.org/10.1175/1520-0493(1987)115<2009:SAAVIT>2.0.CO;2.

Pan, Y., Y. Shen, J. J. Yu, and P. Zhao, 2012: Analysis of the combined gauge-satellite hourly precipitation over China based on the OI technique (in Chinese). *Acta Meteor. Sin.*, **70**, 1381–1389.

Parker, M. D., and R. H. Johnson, 2000: Organizational modes of midlatitude mesoscale convective systems. *Mon. Wea. Rev.*, **128**, 3413–3436, https://doi.org/10.1175/1520-0493(2001)129<3413:OMOMMC>2.0.CO;2.

Pope, M., C. Jakob, and M. J. Reeder, 2008: Convective systems of the north Australian monsoon. *J. Climate*, **21**, 5091–5112, https://doi.org/10.1175/2008JCLI2304.1.

Punkka, A. J., and M. Bister, 2015: Mesoscale convective systems and their synoptic-scale environment in Finland. *Wea. Forecasting*, **30**, 182–196, https://doi.org/10.1175/WAF-D-13-00146.1.

Purdom, J. F. W., and K. Marcus, 1982: Thunderstorm trigger mechanism over the southeast U.S. Preprints, *12th Conf. on Severe Local Storms*, San Antonio, TX, Amer. Meteor. Soc., 487–488.

Rafati, S., and M. Karimi, 2017: Assessment of mesoscale convective systems using IR brightness temperature in the southwest of Iran. *Theor. Appl. Climatol.*, **129**, 539–549, https://doi.org/10.1007/s00704-016-1797-7.

Schumacher, R. S., and R. H. Johnson, 2005: Organization and environmental properties of extreme rain producing mesoscale convective systems. *Mon. Wea. Rev.*, **133**, 961–976, https://doi.org/10.1175/MWR2899.1.

Shen, Y., P. Yang, J. J. Yu, P. Zhao, and Z. J. Zhou, 2013: Quality assessment of hourly merged precipitation product over China (in Chinese). *Daqi Kexue Xuebao*, **36**, 37–46.

Song, F. F., Z. Feng, L. R. Leung, R. A. Houze, J. Y. Wang, J. Hardin, and C. R. Homeyer, 2019: Contrasting spring and summer large-scale environments associated with mesoscale convective systems over the U.S. Great Plains. *J. Climate*, **32**, 6749–6767, https://doi.org/10.1175/JCLI-D-18-0839.1.

Sun, J. H., and Q. F. Zhang, 2012: Impacts of mountain–plains solenoid on diurnal variations of rainfalls along the mei-yu front over the East China plains. *Mon. Wea. Rev.*, **140**, 379–397, https://doi.org/10.1175/MWR-D-11-00041.1.

——, L. L. Zheng, and S. X. Zhao, 2014: Impact of moisture on the organizational mode and intensity of squall lines determined

through numerical experiments (in Chinese). *Chin. J. Atmos. Sci.*, **38**, 742–755.

Takemi, T., 2007: Environmental stability control of the intensity of squall lines under low-level shear conditions. *J. Geophys. Res.*, **112**, D24110, https://doi.org/10.1029/2007JD008793.

Tao, S. Y., 1980: *Heavy Rainfalls in China* (in Chinese). Science Press, 255 pp.

Tollerud, E. I., J. Augustine, and B. D. Jamison, 1992: Cloud top characteristics of mesoscale convective systems in 1986. Preprints, *Sixth Conf. on Satellite Meteorology and Oceanography*, Atlanta, GA, Amer. Meteor. Soc., J3–J7.

USGS, 2003: Global 30-arc-second elevation data set (GTOPO30). U.S. Geological Survey, accessed 22 December 2019, https://doi.org/10.5066/F7DF6PQS.

Wang, S. L., H. W. Kang, X. Q. Gu, and Y. Q. Ni, 2015: Numerical simulation of mesoscale convective system in the warm sector of Beijing ''7.21'' severe rainstorm (in Chinese). *Meteor. Mon.*, **41**, 544–553.

Wilson, J. W., G. B. Foote, N. A. Crook, J. C. Fankhauser, C. G. Wade, J. D. Tuttle, and C. K. Mueller, 1992: The role of boundary-layer convergence zones and horizontal rolls in the initiation of thunderstorms: A case study. *Mon. Wea. Rev.*, **120**, 1785–1815, https://doi.org/10.1175/1520-0493(1992)120<1785:TROBLC>2.0.CO;2.

Xie, L., and K. Ueno, 2011: Differences of synoptic fields depending on the location of MCS genesis in southwest China. *Tsukuba Geoenviron. Sci.*, **7**, 3–12, http://hdl.handle.net/2241/116870.

Xu, W. X., 2013: Precipitation and convective characteristics of summer deep convection over East Asia observed by TRMM. *Mon. Wea. Rev.*, **141**, 1577–1592, https://doi.org/10.1175/MWR-D-12-00177.1.

Xu, X. D., S. Y. Tao, J. Z. Wang, L. S. Chen, L. Zhou, and X. R. Wang, 2002: The relationship between water vapor transport features of Tibetan Plateau-Monsoon ''large triangle'' affecting region and drought-flood abnormality of China (in Chinese). *Acta Meteor. Sin.*, **60**, 257–266.

Yang, Q., R. A. Houze, L. R. Leung, and Z. Feng, 2017: Environments of long-lived mesoscale convective systems over the central United States in convection permitting climate simulations. *J. Geophys. Res. Atmos.*, **122**, 13 288–13 307, https://doi.org/10.1002/2017JD027033.

Yang, R. Y., Y. C. Zhang, J. H. Sun, S. M. Fu, and J. Li, 2018: The characteristics and classification of eastward-propagating mesoscale convective systems generated over the second-step terrain in the Yangtze River Valley. *Atmos. Sci. Lett.*, **20**, e874, https://doi.org/10.1002/asl.874.

——, ——, ——, and J. Li, 2020: The comparison of statistical features and synoptic circulations between the eastward-propagating and quasi-stationary MCSs during the warm season around the second-step terrain along the middle reaches of the Yangtze River. *Sci. China Earth Sci.*, **63**, 1209–1222, https://doi.org/10.1007/s11430-018-9385-3.

Yang, X. R., J. F. Fei, X. G. Huang, X. P. Cheng, L. M. Carvalho, and H. R. He, 2015: Characteristics of mesoscale convective systems over China and its vicinity using geostationary satellite FY2. *J. Climate*, **28**, 4890–4907, https://doi.org/10.1175/JCLI-D-14-00491.1.

Zhang, M. M., and Z. H. Jiang, 2013: Analyses of high-resolution merged precipitation products over China (in Chinese). *Climatic Environ. Res.*, **18**, 461–471.

Zheng, L. L., and J. H. Sun, 2013: Characteristics of synoptic and surface circulation of mesoscale convective systems in dry and moist environmental conditions (in Chinese). *Chin. J. Atmos. Sci.*, **37**, 891–904.

——, ——, X. L. Zhang, and C. H. Liu, 2013: Organizational modes of mesoscale convective systems over central east China. *Wea. Forecasting*, **28**, 1081–1098, https://doi.org/10.1175/WAF-D-12-00088.1.

Zheng, Y. G., and J. Chen, 2013: A climatology of deep convection over South China and the adjacent waters during summer. *J. Trop. Meteor.*, **19**, 1–15.

——, ——, and P. J. Zhu, 2008: Climatological distribution and diurnal variation of mesoscale convective systems over China and its vicinity during summer. *Chin. Sci. Bull.*, **53**, 1574–1586, https://doi.org/10.1007/s11434-008-0116-9.

——, M. Xue, B. Li, J. Chen, and Z. Y. Tao, 2016: Spatial characteristics of extreme rainfall over China with hourly through 24-hour accumulation periods based on national-level hourly rain gauge data. *Adv. Atmos. Sci.*, **33**, 1218–1232, https://doi.org/10.1007/s00376-016-6128-5.